CALIBRATION TECHNIQUE FOR POLARIZATION-SENSITIVE LIDARS

J. M. Alvarez[*], M. A. Vaughan[§], C. A. Hostetler[†], W. H. Hunt[§], and D. M. Winker[†]

[*] *NASA Langley Research Center, Hampton Virginia USA (retired)*

[§] *Science Applications International Corporation (SAIC) , Hampton Virginia USA*

[†] *NASA Langley Research Center, Hampton Virginia USA*

Jose M. Alvarez
NASA Langley Research Center (retired)
313 Pasture Lane
Hampton, VA 23669
phone: 757-723-2401
email: joelarc@verizon.net

Mark A. Vaughan
Science Applications International Corp.
Mail Stop 475
NASA Langley Research Center
Hampton, VA 23681-2199
phone: 757-864-5331
fax: 757-864-2671
email: m.a.vaughan@larc.nasa.gov

Chris A. Hostetler
NASA Science Directorate, Climate Science Branch
Mail Stop 420
NASA Langley Research Center
Hampton, VA 23681-2199
phone: 757-864-5373
fax: 757-864-7996
email: chris.a.hostetler@nasa.gov

William H. Hunt
Science Applications International Corp.
Mail Stop 475
NASA Langley Research Center
Hampton, VA 23681-2199
phone: 757-864-1359
fax: 757-864-2671
email: b.h.hunt@larc.nasa.gov

David M. Winker
NASA Science Directorate, Climate Science Branch
Mail Stop 475
NASA Langley Research Center
Hampton, VA 23681-2199
phone: 757-864-6747
fax: 757-864-7775
email: david.m.winker@nasa.gov

ABSTRACT

Polarization-sensitive lidars have proven to be highly effective in discriminating between spherical and non-spherical particles in the atmosphere. These lidars use a linearly polarized laser and are equipped with a receiver that can separately measure the components of the return signal polarized parallel and perpendicular to the outgoing beam. In this work we describe a technique for calibrating polarization-sensitive lidars that was originally developed at NASA's Langley Research Center (LaRC) and has been used continually over the past fifteen years. The procedure uses a rotatable half-wave plate inserted into the optical path of the lidar receiver to introduce controlled amounts of polarization cross-talk into a sequence of atmospheric backscatter measurements. Solving the resulting system of nonlinear equations generates the system calibration constants (gain ratio, G, and offset angle, θ) required for deriving calibrated measurements of depolarization ratio from the lidar signals. In addition, this procedure also determines the mean depolarization ratio within the region of the atmosphere that is analyzed. Simulations and error propagation studies show the method to be both reliable and well behaved. Operational details of the technique are illustrated using measurements obtained as part of Langley Research Center's participation in the First ISCCP Regional Experiment (FIRE).

1. INTRODUCTION

It is well known that 180-degree backscattering from spherical particles retains the polarization state of the incident beam (Bohren and Huffman, 1983). The depolarization lidar technique makes use of this phenomenon by using a linearly polarized laser transmitter mated to a two-channel receiver capable of measuring the components of the return signal polarized parallel and

perpendicular to the transmitted beam. The signal separation is typically accomplished using a polarizing beam splitter (PBS), which directs the perpendicular-polarized component of the backscatter signal to one channel and the parallel to the other (Sassen, 2000). The calibrated ratio of these two components is known as the depolarization ratio. Depolarization ratio measurements provide information about the shape and/or thermodynamic phase of the particles in the scattering medium (Sassen, 1991), and for this reason they have been widely used and studied within the atmospheric sciences. The depolarization lidar technique dates back to the early 1970s, when the depolarization of backscattered laser light was shown to provide effective discrimination between ice clouds and water clouds (Schotland et al., 1971). Later studies augmented the technique by using depolarization signatures to identify regions of horizontally aligned hexagonal plates in altostratus clouds (Platt 1977). Recent analyses of cirrus clouds have used lidar-measured depolarization ratios to derive the effective shape ratios of cirrus cloud particles (Noel et al., 2002).

Dual polarization lidars are also used to probe other atmospheric constituents. Within the troposphere, polarization-sensitive lidars are frequently used to detect the presence of dust within the planetary boundary layer (Murayama et al., 2001; Gobbi et al., 2000). In the stratosphere, depolarization measurements obtained at 532 nm during the Airborne Arctic Stratospheric Experiment (AASE) contributed significantly to the first morphological classifications of polar stratospheric clouds (PSCs; see Poole et al., 1990). Subsequent analyses of multi-wavelength lidar measurements obtained during the AASE have further extended the utility of depolarization ratio measurements in PSC identification and classification (Toon et al., 2000). Depolarization ratios have also been used to identify and distinguish between volcanic ash and sulfuric acid droplets in the stratospheric aerosol plume produced by the eruption of Mt. Pinatubo in 1991

(Winker and Osborn, 1992). In the near future, depolarization measurements are expected to play a pivotal role in the fully automated scene classification and feature identification algorithms being developed for the Cloud-Aerosol Lidar and Infrared Pathfinder Satellite Observations (CALIPSO) mission (Winker et al., 2002; Hu et al., 2001; Omar et al., 2003).

The key to deriving accurate measurements of depolarization ratio lies in obtaining a reliable calibration of the receiver channels. This work presents a technique that determines the system depolarization calibration constants while simultaneously retrieving an estimate of the mean volume depolarization ratio within the region of the atmosphere over which the calibration constants are computed. In section 2 we derive the basic depolarization equation for an ideal lidar system, and introduce the depolarization gain ratio, which quantifies the relative magnitudes of the combined optical and electrical gains of the parallel and perpendicular receiver channels. Previously published techniques for retrieving the gain ratio are reviewed in section 3. In section 4 we describe modifications to both the lidar hardware and the depolarization equation that form the basis for our calibration technique. In this section we also introduce the transmitter-to-receiver offset angle, which parameterizes cross-talk between the two receiver channels, and describe the mechanics of the calibration technique. Measurement accuracy issues and uncertainty analyses are explored in sections 5 and 6. Practical considerations for implementing the technique, illustrated using a real-world example, are given in section 7. Section 8 concludes the paper with a recap of the most important aspects of the method.

2. DEVELOPING THE DEPOLARIZATION EQUATION

Following the development given by Measures (1984), the single-scattering approximation for the total optical power backscattered from range r into the receiver of an elastic backscatter lidar is given by

$$P(r) = P_0 \cdot A \cdot \xi(r) \cdot \zeta \cdot \frac{c \cdot t_L}{2} \cdot \frac{1}{r^2} \cdot \beta(r) \cdot T^2(r). \quad (1)$$

The first five terms in this equation describe design characteristics of the lidar. P_0 is the average laser pulse power ($P_0 = E_0 / t_L$, where E_0 is the initial laser pulse energy and t_L is the laser pulse width). A is the effective area of the telescope mirror, ζ characterizes the spectral transmission efficiencies of the transmitter and receiver at the laser wavelength, and c is the speed of light. $\xi(r)$ is an overlap factor describing the degree to which the laser beam fills the receiver's field of view. For this work we assume that measurements are made far from the receiver using a properly bore-sighted system, so that $\xi(r) \equiv 1$. The final two terms in the equation quantify the interaction between the propagating laser energy and the atmosphere through which it travels. $\beta(r)$ is the volume backscatter coefficient, and $T^2(r)$ is the two way transmittance of the atmosphere. Combining terms, we can rewrite the lidar equation in a simplified form as

$$P(r) = E_0 \cdot \frac{C}{r^2} \cdot \beta(r) \cdot T^2(r) \quad (2)$$

where (recalling that $\xi(r) \equiv 1$) $C = \frac{1}{2} \cdot A \cdot \zeta \cdot c$.

The digitized signal, Q, stored by the lidar data acquisition subsystem is proportional to the received optical power, P; that is, $Q = \mathcal{g} \cdot P$, where $\mathcal{g}$ is parameterizes the electro-optic gain of the receiver and includes factors such as transmission optics losses, detector electronics gain, electro-optic conversion coefficients (e.g., photo-multiplier quantum efficiencies), and the electronic gain of any preamplifiers. In an ideal system, the processes involved in converting backscattered laser light into a series of digitized signals are all linear, and thus the equations representing the signals stored in the parallel $(\|)$ and perpendicular $(\perp)$ channels of the data acquisition sub-system can be written as

$$Q_{\|}(r) = \mathcal{g}_{\|} \cdot E_0 \cdot \frac{C}{r^2} \cdot \beta_{\|}(r) \cdot T^2(r) \tag{3a}$$

and

$$Q_{\perp}(r) = \mathcal{g}_{\perp} \cdot E_0 \cdot \frac{C}{r^2} \cdot \beta_{\perp}(r) \cdot T^2(r). \tag{3b}$$

Here $Q_{\|}(r)$ and $Q_{\perp}(r)$ represent the range-resolved digitized signals and the $\mathcal{g}_{\|}$ and $\mathcal{g}_{\perp}$ terms quantify the electro-optic signal gain for each channel incurred after the beam passes through the PBS. The volume backscattering coefficients for the parallel and perpendicular polarizations are given by $\beta_{\|}(r)$ and $\beta_{\perp}(r)$, respectively. For typical dual polarization lidars, the digitized parallel and perpendicular signals share several factors in common. In particular, both the r^2 term and the two-way transmittance of the atmosphere, $T^2(r)$, make identical contributions to both signals. We also explicitly assume that the optical efficiencies of all components before the

half-wave plate are essentially identical for both polarization orientations, so that the system constant term, C, is also identical for both channels. This requirement should not be unduly restrictive, as it is fulfilled by those systems for which the components within the optical path are all aligned with a zero-degree angle of incidence. If we further assume that the polarization planes of the transmitter and receiver are in perfect alignment, we can define the measured ratio of the two signals as

$$m(r) = \frac{Q_{\perp}(r)}{Q_{\parallel}(r)} = \frac{\mathcal{G}_{\perp} \cdot C/r^2 \cdot E_0 \cdot T^2(r) \cdot \beta_{\perp}(r)}{\mathcal{G}_{\parallel} \cdot C/r^2 \cdot E_0 \cdot T^2(r) \cdot \beta_{\parallel}(r)} = \left(\frac{\mathcal{G}_{\perp}}{\mathcal{G}_{\parallel}}\right) \cdot \left(\frac{\beta_{\perp}(r)}{\beta_{\parallel}(r)}\right) = G \cdot \delta(r), \tag{4}$$

where $G = \mathcal{G}_{\perp}/\mathcal{G}_{\parallel}$ is the depolarization gain ratio, and $\delta(r) = \beta_{\perp}(r)/\beta_{\parallel}(r)$ is the volume depolarization ratio. In this idealized case, all that is necessary to retrieve the depolarization ratios from the measured ratios is an accurate estimate of the depolarization gain ratio, G.

In closing this section we note that the definition for depolarization ratio adopted in this work is not universally employed. A comprehensive overview of the several different depolarization ratio definitions used within the lidar community can be found in Cairo et al., 1999.

3. EXISTING TECHNIQUES FOR ESTIMATING GAIN RATIO

Gain ratio calibrations are frequently accomplished by normalizing the measured ratios in a region of "clear air" (i.e., a region assumed to consist of purely molecular scatterers) to some theoretically appropriate value for the molecular depolarization ratio (e.g., Sauvage et al, 1999; Beyerle et al, 2001). Using this technique, an estimate of the gain ratio, $\hat{G}$, is obtained using

$\hat{G} = \langle m_{clear} \rangle / \delta_{target}$, where $\langle m_{clear} \rangle$ is the mean measured ratio computed over the presumed-to-be-clear region of the atmosphere, and δ_{target} is the molecular depolarization ratio that should be measured by the system being calibrated. The exact value of δ_{target} to be used depends on the optical architecture of the system, and, if the filter line-width is broad enough to include the rotational Raman bands, the temperature of the atmosphere in the calibration region (Behrendt and Nakamura, 2002). Successful calibration of a dual-polarization lidar via the clear air normalization method therefore requires an accurate and precise knowledge of the filter band-pass characteristics. For very narrow filters, the contributions to δ_{target} are restricted to Cabannes scattering ($\delta_{target} = 0.00365$). If the filter line width is substantially broader, a Rayleigh scattering model (Cabannes + rotational Raman contributions) may be required (She, 2001), and in this case δ_{target} is larger by a factor of ~4 (Biehle et al., 2000). Intermediate line widths will of course require intermediate values of δ_{target}.

A second method for deriving the gain ratio is exemplified by the procedure described in Spinhirne, et al. (1982). At the cost of some additional hardware, this technique obviates the requirement for an exact a priori knowledge of δ_{target}. Spinhirne's procedure uses a half-wave plate inserted into the optical path of the transmitter to rotate the polarization plane of the laser output by 45º with respect to the polarization axis of the receiver. Assuming the polarization planes of the transmitter and receiver are perfectly aligned, signals of equal backscatter intensity will then be measured by each receiver channel, irrespective of the scattering medium being sampled. A modified version of the Spinhirne procedure, one that places the half-wave plate in the receiver rather than the transmitter, is used by McGill et al. (2002).

The requirement for a priori knowledge of δ_{target} is also eliminated by the gain ratio calibration technique used by Sassen et al. (2001). In this method, equal input signals are generated by placing an unpolarized light source at the minimum telescope focus. The gain ratio is then retrieved from the ratio of the measured outputs.

A somewhat different approach to the gain ratio calibration issue was taken by Platt (1977). Polarization optics installed in the receiver were designed to be rotated fully between successive laser pulses, allowing for interleaved acquisition of the parallel and perpendicular signals. As only a single detector and data acquisition channel is used in this scheme, the gain ratio is unity by definition, and the requirement for a gain ratio calibration vanishes, albeit at the price of non-simultaneous measurements of the polarization components. The single-detector technique has also been employed by Eloranta & Piironen (1994), who used a Pockels cell to rotate the polarization plane of the laser transmitter by 90° between successive pulses. The pulse repetition frequency of their system is 4 kHz, versus the 1 Hz system used by Platt, and thus the effects of non-simultaneous measurements are largely eliminated.

4. IMPROVED CALIBRATION TECHNIQUE

4.1. ACCOUNTING FOR INSTRUMENT ALIGNMENT ERRORS

The development of equation (4) assumes that the polarization planes of the transmitter and receiver are in perfect alignment. In a perfectly aligned system equipped with an ideal linearly polarized laser, the polarization plane of the laser is exactly parallel to the parallel axis of the PBS. Given such a system, the measured ratios generated by single scattering from perfectly

spherical particles will be zero. Suppose, however, that the optical axis of the polarizing cube is somewhat misaligned with that of the transmitted beam. This misalignment induces a degree of polarization cross-talk into the measured ratios – i.e., some fraction of the parallel signal is leaked into the perpendicular channel (and vice versa), thereby contaminating the measurements from which the depolarization ratios are ultimately derived. The effects of this contamination are examined in detail below in section 6. In the current section we describe the physical modifications to the lidar that allow us to compensate for potential alignment errors, and develop the corresponding physical and mathematical formulations.

As noted earlier, the alignment of the transmitting and receiving polarization axes can be adjusted by use of a half-wave plate. The polarization-sensitive lidars used by our research group are therefore equipped with a half-wave plate installed in the optical path of the receiver. A simplified schematic showing the relevant design features is presented in Figure 1. More detailed descriptions of various LaRC systems can be found in Winker and Osborn (1992), Winker and Vaughan (1994), and DeCoursey et al. (1996). With respect to polarization calibration, the key component characterizing all of these instruments is a zero-order half-wave plate mounted in the receiver optical train immediately upstream of the primary PBS. Rotation

of the half-wave plate is controlled using a motor-driven rotational mount that can be commanded to high angular precision via a computerized interface.[1]

Also critical, both to calibrating the instrument and to subsequent depolarization ratio measurements, is the insertion of a secondary PBS to ensure the polarization purity of the perpendicular polarization channel. Manufacturer specifications for commercially available PBS cubes typically quote extinction ratios of better than 1000 to 1, with transmission efficiencies of $T_P > 95\%$, and reflection efficiencies of $R_S > 99.9\%$.[2] With respect to measurement accuracy, the ~5% transmission loss in the parallel component is of particular concern. While some of this transmission loss occurs through attenuation in the proprietary, multi-layer interface between the two halves of the polarizing cube, the remainder of the energy, estimated at 2% to perhaps 3%, is erroneously included in the reflected component. However, the electric field vector of this renegade P-channel energy vibrates at right angles to the desired S-component of the signal. The second PBS will therefore transmit ~95% of the desired S-channel signal, and attenuate the P-channel contamination by a factor of ~1000. The polarization purity of the signals incident on the detectors in this paired-PBS configuration is thus 950:1 or better for both channels. Recent

---

[1] The polarization sensitive lidar flown as part of the SAGE III Ozone Loss and Validation Experiment (SOLVE; Newman et al., 2002), uses a zero-order half-wave plate from VLOC (http://www. vloc.com), part number WZH381-0532-2000, and an Oriel (http://www.oriel.com/) model 13048 motorized rotator together with an Oriel model 18011 encoder mike controller.

[2] As of July 25, 2005, CVI Lasers quotes these exact specifications for their PBS-532-100 polarizing beamsplitter cube; see http://www.cvilaser.com.

conversations with manufacturers' representatives of confirm that this method remains the preferred way to deal with PBS cross-talk (Hull, 2005).

Given a properly configured lidar, we define the global polarization frame of reference to coincide with the polarization axes of the primary PBS. Maintaining our assumption of perfect optical alignment, the polarization plane of the transmitter is exactly matched to the principle axis of the half-wave plate, and the principle axis of the half-wave plate is likewise perfectly parallel to the polarization plane of the PBS. In this case, the orientation of the polarization components of the signal backscattered from a non-depolarizing target (e.g., single-scattering from perfect spheres) will be as illustrated on the left side of Figure 2. Because the angle between the polarization plane of the backscattered laser light and the principle axis of the half-wave plate is zero, the intensities of both the parallel and perpendicular components of the backscattered light are transmitted without change to the PBS, and the corresponding measured ratios will be zero.

Now consider the more general case, in which the polarization planes of the transmitter and receiver are no longer perfectly aligned. We parameterize the magnitude and direction of the misalignment between transmitter and receiver by defining a systematic offset angle, θ. Under these conditions, if we were to remove the half-wave plate from the optical path, the geometry of the signal backscattered from a non-depolarizing target would be as illustrated in the center of Figure 2. Reinserting the wave plate with its principal axis co-aligned with the parallel axis of the PBS, the polarization state of the light after transmission through the wave plate is now rotated with respect to its original state by a factor of 2θ (Hecht, 2002). This final configuration

is shown in the right-hand panel of Figure 2. The corresponding electric field vectors for the parallel and perpendicular components incident on the PBS are given by

$$\mathcal{E}_{t,\parallel} = \mathcal{E}_{i,\parallel} \cdot \cos(2\theta) + \mathcal{E}_{i,\perp} \cdot \sin(2\theta) \tag{5a}$$

$$\mathcal{E}_{t,\perp} = \mathcal{E}_{i,\perp} \cdot \cos(2\theta) - \mathcal{E}_{i,\parallel} \cdot \sin(2\theta) \tag{5b}$$

where $\mathcal{E}_t$ represents the field transmitted through the half-wave plate, $\mathcal{E}_i$ represents the incident field, and θ is the offset angle. Since the electric fields produced by the scattering process are assumed to be uncorrelated, the time-averaged cross products vanish and the powers associated with the transmitted fields are

$$P_{\parallel} = \tfrac{1}{2} \cdot \left(\mathcal{E}_{i,\parallel}^{\,2} \cdot \cos^2(2\theta) + \mathcal{E}_{i,\perp}^{\,2} \cdot \sin^2(2\theta) \right) \tag{6a}$$

$$P_{\perp} = \tfrac{1}{2} \cdot \left(\mathcal{E}_{i,\parallel}^{\,2} \cdot \sin^2(2\theta) + \mathcal{E}_{i,\perp}^{\,2} \cdot \cos^2(2\theta) \right) \tag{6b}$$

Recognizing that $\mathcal{E}_i^2 = K \cdot \left(C / r^2 \right) \cdot E_0 \cdot T^2 \cdot \beta$, where K is a constant of proportionality, we can substitute (6a) and (6b) into (4) and write the expressions for the signals received in the parallel and perpendicular channels as

$$Q_{\parallel} = \tfrac{1}{2} \cdot \left(K \cdot \frac{C}{r^2} \cdot E_0 \cdot T^2 \cdot g_{\parallel} \cdot \left(\beta_{\parallel} \cdot \cos^2(2\theta) + \beta_{\perp} \cdot \sin^2(2\theta) \right) \right) \tag{7a}$$

$$Q_{\perp} = \tfrac{1}{2} \cdot \left(K \cdot \frac{C}{r^2} \cdot E_0 \cdot T^2 \cdot \mathcal{G}_{\perp} \cdot \left(\beta_{\parallel} \cdot \sin^2(2\theta) + \beta_{\perp} \cdot \cos^2(2\theta) \right) \right) \tag{7b}$$

Using the terms given in (7) we can derive the measured ratios as a function of gain ratio, depolarization ratio, and offset angle:

$$m = \frac{Q_{\perp}}{Q_{\parallel}} = \frac{\mathcal{G}_{\perp} \cdot \left(\beta_{\parallel} \cdot \sin^2(2\theta) + \beta_{\perp} \cdot \cos^2(2\theta) \right)}{\mathcal{G}_{\parallel} \cdot \left(\beta_{\parallel} \cdot \cos^2(2\theta) + \beta_{\perp} \cdot \sin^2(2\theta) \right)} \tag{8}$$

Factoring common terms and making the range dependence explicit yields a revised depolarization equation, which accounts for the effects of a systematic offset angle:

$$m(r) = G \cdot \left(\frac{\delta(r) + \tan^2(2\theta)}{1 + \delta(r) \cdot \tan^2(2\theta)} \right) \tag{9}$$

For a system with an offset angle of zero, equation (9) reduces, as expected, to equation (4). More importantly, it is clear from equation (9) that if the offset angle is known, the polarization components of the system can be brought into alignment by the appropriate rotation of the half-wave plate.

4.2. SIMULTANEOUS RETRIEVAL OF GAIN RATIO AND OFFSET ANGLE

Calibration data is accumulated by acquiring a fixed number of lidar profiles at each of a sequence of accurately measured calibration angles. Calibration angles are measured relative to the position of the half-wave plate at the start of the procedure, and obtained by rotating the half wave plate. For the profiles acquired at any angle, the *effective offset angle* is thus the sum of the

actual systematic offset angle, θ, and the current calibration angle, φ. Repeating the rotation process for three or more calibration angles generates a set of backscatter profiles into which we have introduced controlled amounts of polarization cross-talk. The amount of cross-talk varies from angle to angle, but remains constant within the data acquisition sequence for each separate angle. Hence for the j^{th} calibration angle, φ_j, the equation describing the range-resolved measured ratios becomes

$$m_j(r) = G \cdot \left(\frac{\delta(r) + \tan^2\left(2\left(\theta + \varphi_j\right)\right)}{1 + \delta(r) \cdot \tan^2\left(2\left(\theta + \varphi_j\right)\right)} \right) \tag{10}$$

where $m_j(r)$ and φ_j are measured (and thus known) values and $\delta(r)$, G, and θ are the parameters to be estimated by the calibration procedure. Because the calibration equation contains three unknowns, backscatter data must be acquired at a minimum of three calibration angles. A nonlinear least squares algorithm is then applied to solve the resulting (range-resolved) systems of equations over some region of the data for which the measured ratios remain essentially constant.

It is important to reiterate here that, in addition to calculating the gain ratio and the offset angle, this procedure also determines the volume depolarization ratios within the selected altitude range. Unlike the clear air normalization technique, we specifically do not require an accurate a priori estimate of δ_{target}, nor in principal do we require a purely molecular calibration region (but see section 7 for some practical caveats). Among published calibration techniques, only the method advocated by Sassen et al. (2001) explicitly recognizes and attempts to correct for the effects of misalignment between the transmitter and the receiver. Sassen defines the

depolarization ratio using $\delta(r) = G \cdot m(r) - \chi$, where χ "is a correction factor accounting for the imprecise alignment between the laser E vector and the orientation plane of the receiver polarizing prism, as well as any randomness in the transmitted laser pulse polarization properties". However, while Sassen's technique avoids using δ_{target} in ascertaining the system gain ratio (i.e., as in section 3), δ_{target} is nonetheless required for the practical determination of χ (i.e., $\delta_{target} = G \cdot m(r) - \chi$, where G is known, m(r) is measured, and χ is the only unknown).

5. ERROR ANALYSIS I: CALIBRATION COEFFICIENT UNCERTAINTIES

The depolarization calibration coefficients are retrieved by solving a nonlinear least squares problem. While deriving a general error analysis for nonlinear least squares problems can be quite difficult, error estimates for any specific solution can be obtained using the final approximation to the Hessian matrix generated by the nonlinear least squares solver (e.g., Cox, Forbes, & Harris, 2004). However, estimating errors using this technique relies on the assumption that the noise in the inputs can be characterized as additive, zero-mean, and Gaussian-distributed, with an identical variance for all parameters (Frieden, 2001). Therefore, a more accurate and intuitive understanding of the correlations between input uncertainties and output errors is often best obtained by Monte Carlo simulations (Press, et al., 1992; Anita, 2002). In the sections below we describe numerical experiments that benchmark the performance and stability of the retrieval technique, and provide heuristics for assessing calibration coefficient uncertainties as a function of measured signal-to-noise ratio (SNR) and the number of calibration angles used (N_φ).

5.1. MONTE CARLO SIMULATION DESIGN

Our investigation of error propagation was conducted using simulation software designed to reproduce all relevant characteristics of the depolarization calibration process. Using equations (3a) and (3b), synthetic lidar backscatter signals are generated for both the parallel $\left(P_{\parallel}\right)$ and perpendicular $\left(P_{\perp}\right)$ channels. When deriving these signals, the system gain ratio and offset angle, the atmospheric depolarization ratio, and the SNR of the laser backscatter are all fully configurable for each trial. User-specified noise levels in the simulated backscatter signals are introduced via a Poisson-distributed random number generator. The number and magnitude of the angles used in any calibration are also user-configurable. Errors in the calibration angle measurements due to backlash and/or hysteresis are modeled as normally distributed, with distribution parameters obtained from specifications provided by the manufacturer(s) of the rotational stage and its associated controller. Solutions to the non-linear least squares problem are generated from the derived measured ratios using an implementation of a damped Gauss-Newton method adapted from Dennis and Schnabel (1996). All software was written in Object Pascal, using Borland's Delphi compiler.

Calibration constant errors were characterized using two separate Monte Carlo simulations. The first of these concentrated on SNR and N_{φ} effects only, and thus the calibration angles were assumed error-free. In the second, realistic rotator uncertainties were added to the calibration angles. Both studies examined the effects of variability originating in three domains: backscatter SNR, which is defined with respect to total optical intensity immediately prior to the PBS cube; the number of calibration angles used; and the target (i.e., "truth") values for gain ratio, offset angle, and molecular depolarization ratio. For each study, calibration constants were derived

from 200,000 independently generated sets of simulated measured ratios. Twenty-five back-scatter SNR levels were specified, ranging from 10 to 250 in increments of 10. The number of angles used at each SNR level was varied from the required minimum of 3 to a maximum of 10. Reasonable, physically meaningful ranges were established for the depolarization calibration constants and the clear air depolarization ratio, as follows:

- $1.0 < G < 4.0$ – Gain ratio limits were chosen based on dynamic range considerations. For example, for a typical cirrus cloud volume depolarization ratio of 0.50, the optical intensity measured in the perpendicular channel is one-half of the intensity measured in the parallel channel. The perpendicular channel gain can therefore be increased accordingly, yielding a gain ratio of 2. As aerosols (excluding larger dust particles) generally have much lower depolarization ratios than cirrus clouds, aerosol measurements could presumably use gain ratios as high as 4.

- $-2.0° < \theta < 2.0°$ – Experience has shown that the offset angle can be set to within ±2.0° via visual inspection of the backscatter signal; that is, by rotating the half wave plate so that the magnitude of the perpendicular return is minimized in the target calibration region.

- $0.0037 < \delta < 0.0288$ – This range extends from Cabannes depolarization at the lower end to twice Rayleigh depolarization at the upper end.

For each of the 200 combinations of SNR and N_φ, 1000 sets of simulated measured ratios were generated. Each set of measured ratios was constructed using a separate $\{G, \delta, \theta\}$ "truth vector"

that was produced using a uniform random number generator scaled to the ranges specified above for each parameter. The nonlinear least squares problem was then solved for each set, yielding a three-element solution vector, $\{\tilde{G}, \tilde{\delta}, \tilde{\theta}\}$. For each vector element and each {SNR, N_φ} pair, we then compute the root-mean-square (RMS) deviation of the retrieved value, $\tilde{X}$, from the simulated target value, X, using

$$\mathrm{RMS}(X) = \sqrt{\frac{1}{1000}\sum_{i=1}^{1000}\left(X_i - \tilde{X}_i\right)^2}\,. \tag{11}$$

Here X can be either G, δ, or θ. When computed according to equation (11), the depolarization ratio error metric is returned as a percentage, the offset angle error metric has units of degrees, and the gain ratio error metric is unitless.

The values of the calibration angles used for each N_φ trial are listed in Table 1. The maximum range of angles that can be used is confined to ±22.5º about true zero, as beyond this limit the polarization sensitivity of the two receiver channels is effectively swapped. In practice we have found that, due to the low SNR of the measured ratios, a calibration angle of zero is unsuitable for daytime calibrations using a molecular region of the atmosphere. Accordingly, the range of calibration angles was chosen to be between ±20°, excluding the subrange of ±4º.

5.2. MONTE CARLO SIMULATION RESULTS AND DISCUSSION

In Figure 3 we present contour plots displaying the RMS errors for gain ratio (left side) and offset angle (right side) obtained from the Monte Carlo simulation using error-free calibration angles. These plots display contours of constant RMS error as a function of both SNR (log scale,

vertical axis) and N_φ (linear scale, horizontal axis). Each contour line is labeled with its corresponding RMS error value. The gain ratio errors are seen to depend strongly on backscatter SNR, but have only a weak dependence on the number of calibration angles used. That the gain ratio retrieval is relatively insensitive to N_φ is not surprising, as the calibration equation is linear with respect to G. N_φ exerts a noticeably larger influence on the RMS errors for the offset angle. However, for both gain ratio and offset angle, the error metric decreases exponentially with increasing SNR, whereas the decrease with increasing numbers of calibration angles is approximately linear. The actual errors retrieved in the simulation are show using solid red lines. The dashed black lines show the predicted errors obtained from two-dimensional linear approximating functions of the form $y = C_0 \cdot \mathrm{SNR}^{C_1} \cdot e^{C_2 \cdot N_\varphi}$, where, as previously defined, SNR is the backscatter signal-to-noise ratio and N_φ represents the number of calibration angles. The RMS error in the gain ratio as a function of SNR and N_φ can therefore be approximated using

$$\Delta G\left(N_\varphi, \mathrm{SNR}\right) = 4.695 \cdot \mathrm{SNR}^{-1.026} \cdot e^{-0.014 \cdot N_\varphi}. \tag{12}$$

Similarly, the RMS error in the offset angle is approximated by

$$\Delta\theta\left(N_\varphi, \mathrm{SNR}\right) = 13.306 \cdot \mathrm{SNR}^{-1.010} \cdot e^{-0.057 \cdot N_\varphi} \tag{13}$$

where the return value of the $\Delta\theta$ function has units of degrees.

For the second phase of the Monte Carlo study, each of the calibration angles was contaminated with a normally distributed random error having a mean value of zero and a standard deviation of 38.3 microradians. This value is consistent with manufacturer-supplied specifications a motor-

driven rotational stage. The increased output error due to this additional uncertainty in the calibration input data is approximated using a two-dimensional quadratic of the form

$$\ln\left(\Delta X_{\text{Rotator}}\right) = K_0 + K_1 N_\varphi + K_2 \,\text{SNR} + K_3 N_\varphi^{\,2} + K_4 \,\text{SNR}^2 . \tag{14}$$

The quantity denoted by $\Delta X_{\text{Rotator}}$ represents the magnitude of the errors derived in the second simulation divided by the corresponding errors obtained in the first simulation (i.e., the "no rotator error" case). Equation (14) therefore represents an error amplification term that is applied to the original error estimates derived using equations (12) and (13), so that the composite error is given by $\Delta X_{\text{Total}}\left(N_\varphi, \text{SNR}\right) = \Delta X_{\text{Rotator}}\left(N_\varphi, \text{SNR}\right) \cdot \Delta X\left(N_\varphi, \text{SNR}\right)$. Contour plots showing the actual errors (solid red lines) and the errors predicted using the revised approximation functions (dashed black lines) are shown in Figure 4. Coefficients for the additional error in the gain ratio retrieval due to rotator uncertainty are given in equation (15); coefficients for the additional offset angle error are given in equation (16).

$$\Delta G_{\text{Total}}\left(N_\varphi, \text{SNR}\right) = \left(0.831 \cdot e^{\,0.038 N_\varphi + 0.012\,\text{SNR} - 3.85\times10^{-3} N_\varphi^{\,2} - 1.858\times10^{-5}\,\text{SNR}^2}\right) \cdot \Delta G\left(N_\varphi, \text{SNR}\right) \tag{15}$$

$$\Delta \theta_{\text{Total}}\left(N_\varphi, \text{SNR}\right) = \left(0.756 \cdot e^{\,0.019 N_\varphi + 0.013\,\text{SNR} - 1.711\times10^{-3} N_\varphi^{\,2} - 1.921\times10^{-5}\,\text{SNR}^2}\right) \cdot \Delta \theta\left(N_\varphi, \text{SNR}\right) \tag{16}$$

The Monte Carlo studies reported here have been augmented by numerous additional simulation experiments. In these studies we assigned fixed values for G, δ, and θ, then varied the backscatter SNR, the number of angles, and/or the rotator uncertainty in a systematic way, deriving a new set of calibration constants for each change in input parameters. A typical example of the results obtained is shown in Figure 5, where we plot the mean retrieved parameter values as discrete symbols, and the error envelopes, representing ±1 standard

deviation about the respective means, using different line styles. The exponential decrease in the errors associated with all three parameters as a function of increasing SNR is a uniform characteristic of the retrieval. Similarly, within any calibration test, the error envelope for the gain ratio is always the smallest, and the error envelope for the depolarization ratios is always the largest.

6. ERROR ANALYSIS II: DEPOLARIZATION MEASUREMENTS

Because they are essential for the derivation of important geophysical information (i.e., volume depolarization ratios) from subsequent lidar measurements, the primary outputs from the calibration are the two system constants, G and θ. In this section we characterize the effects that uncertainties in these constants will have on the retrieved depolarization ratios. For comparison purposes, we also demonstrate the nature and magnitude of the errors incurred when the offset angle term is ignored (e.g., when the lidar is calibrated using molecular normalization).

6.1. PROPAGATION OF ERROR FOR UNCERTAIN CALIBRATION CONSTANTS

We begin by rearranging (9) to express the volume depolarization ratios in terms of the offset angle, the gain ratio, and the measured ratios, as shown in equation (17):

$$\delta(r) = \frac{m(r) - G\tan^2(2\theta)}{G - m(r)\tan^2(2\theta)}. \qquad (17)$$

Applying a standard propagation of errors (Bevington & Robinson, 1992) to (17) yields

$$\frac{\mathrm{Var}(\delta)}{\delta^2} = F(\theta)\left(G^2\,\mathrm{Var}(m) + m^2\,\mathrm{Var}(G) + 16\left(\frac{\tan(2\theta)}{\tan^2(2\theta)-1}\right)^2 \left(m^2 - G^2\right)^2 \mathrm{Var}(\theta)\right), \quad (18)$$

where

$$F(\theta) = \left(\frac{\tan^4(2\theta)-1}{\left(m\tan^2(2\theta)-G\right)\left(m-G\tan^2(2\theta)\right)}\right)^2 = \frac{\left(1+\delta\tan^2(2\theta)\right)^4}{\delta^2 G^4\left(\tan^4(2\theta)-1\right)^2} \quad (19)$$

and $\mathrm{Var}(x)$ represents the variance of the random variable x, so that the uncertainty or relative error ascribed to x is given by $\sqrt{\mathrm{Var}(x)\,/\,x^2}$. For an offset angle of 0, $F(0) = 1/m^2 G^2$ and (as expected) $\left.\frac{\mathrm{Var}(\delta)}{\delta^2}\right|_{\theta=0} = \frac{\mathrm{Var}(m)}{m^2} + \frac{\mathrm{Var}(G)}{G^2}$. Uncertainties in the depolarization ratio measurements are therefore minimized by maintaining a near zero offset angle, minimizing uncertainties in the gain ratio, and maximizing the signal-to-noise ratio of the measured ratios. These relationships are illustrated in Figure 6, which shows the relative error in the derived depolarization ratio as a function of uncertainties in offset angle and gain ratio for offset angles of 0.1°, 1.0°, and 2.5°. On the assumption that signal averaging can reduce the random error in the measured ratios to an arbitrary level, the SNR for the measured ratios was fixed at 50 for all plots. The gain ratio was fixed at 2.0, and the depolarization ratio at 0.0144. Comparing the plots clearly reveals the deleterious effects of a non-zero offset angle for low depolarization ratio measurements. Given a gain ratio uncertainty of 5% and an offset angle uncertainty of 10%, an offset angle of 2.5° yields a depolarization ratio uncertainty that is more than a factor of 2 higher than what would be measured using an offset angle of 0.1° (13% relative error vs. 5.4% relative

error). However, as the depolarization ratio of the target increases, the disparity between the errors as a function of offset angle decreases.

6.2. EFFECTS OF NEGLECTING OFFSET ANGLE

In addition to the errors described above, calibrations and calculations that neglect the effects of receiver-transmitter misalignment can also incur errors via the gain ratio calibration process. Figure 7(a) shows the gain ratios that would be computed using the molecular normalization technique for an ideal system having a narrow band filter (dashed line, $\delta_{theory} = 0.00365$) and a second ideal system having a broad band filter (solid line, $\delta_{theory} = 0.0144$). For each offset angle shown, the appropriate measured ratios were computed using equation (9). The corresponding gain ratios were then derived using the molecular normalization technique (i.e., via equation (4)). While offset angles close to zero have little effect on the gain ratio retrieval, larger angles lead to substantial errors. The sensitivity of the gain ratio retrieval to offset angle errors is also shown to be a function of the filter line width, which governs the appropriate choice for δ_{theory}. When using the molecular normalization technique to determine the depolarization gain ratio, an offset angle of 1° induces a gain ratio error of ~9% for a system having a filter width for which Rayleigh scattering is the appropriate model. For narrow band filters using a Cabannes scattering model, the error at 1° rises to ~33%.

Even if the gain ratio could be determined exactly, failure to consider the offset angle can still introduce errors whenever equation (4) is used to compute depolarization ratios from the measured ratios. We illustrate this in Figure 7(b). The dashed line shows the relative error in depolarization ratios, $e = \left(\delta_{\text{retrieved}} - \delta_{\text{target}}\right) \big/ \delta_{\text{target}}$, for $\delta_{\text{retrieved}}$ obtained using equation (4) applied

to a system having an offset angle of 1°. The measured ratios were computed using equation (9); a gain ratio of 1.0 was used both to compute the measured ratios and to derive $\delta_{retrieved}$. The relative errors in this case are especially acute for lower values of depolarization, but asymptote to very small values as the particulate depolarization grows larger. The more likely error scenario is shown by the solid line in Figure 7(b). Once again, the measured ratios were computed using equation (9) and a gain ratio of 1.0. However, for this calculation, $\delta_{retrieved}$ was calculated using the gain ratio that would be obtained via the molecular normalization technique: i.e., G = 1.085. In this case, the retrieved depolarization ratios are seen to asymptote to values that are ~8.5% lower than the true values.

7. PRACTICAL CONSIDERATIONS ILLUSTRATED WITH A REAL-WORLD EXAMPLE CALIBRATION

In this section we describe the sequence of procedures required to successfully calibrate a polarization-sensitive lidar. Practical considerations involved in these procedures are illustrated using data acquired by the LaRC dual polarization cloud lidar during the First ISCCP Regional Experiment (FIRE) in Parsons, Kansas (Starr et al, 1990).

7.1. SELECTING THE CALIBRATION REGION

When initiating the calibration, we first identify a region of the atmosphere where the scatterers remain both spatially homogenous and temporally invariant throughout the calibration sequence. Because this condition is rarely, if ever, met in cloud or aerosol layers, calibrations are almost always done in those regions that most resemble 'clear air'. This clear air region need not be

purely molecular; however, any background aerosol present must be uniformly distributed, both spatially and temporally. Using clear air also eliminates possible contamination of the calibration data by multiple scattering.

Figure 8 shows the measured ratios as a function of altitude for a 10-angle calibration acquired on 12 November 1991. The observer log for this date remarks on the exceptionally clear and stable air mass present at the time, conditions borne out by the consistently flat slopes (with respect to altitude) of the measured ratios. The calibration was conducted in full daylight, beginning at approximately 3:05 PM local time. For each calibration angle, the measured ratios shown represent an average accumulated over a one minute sampling interval (600 laser pulses). Following the data acquisition sequence, the parallel and perpendicular channel data were time-averaged to form a single pair of profiles for each calibration angle, $P_{\parallel}(\theta_j, r)$ and $P_{\perp}(\theta_j, r)$. The data shown in Figure 8 are computed by forming the ratio of these two profiles; that is, $m_j(r) = P_{\perp}(\theta_j, r) / P_{\parallel}(\theta_j, r)$.

The upper and lower altitudes that define the altitude regime over which the calibration will be computed are chosen based on a single selection criterion: for all angles, the measured ratios within the region must be constant (to within the expectation of the SNR of the measurements). Satisfying this requirement is essential for assuring the spatial homogeneity of the calibration region. In selecting the calibration altitude range, practitioners should also be cognizant of the temperature dependence of the molecular volume depolarization ratio, as described in Behrendt and Nakamura (2002). For certain filter line widths, selecting too broad a temperature range can encompass a natural variation in molecular depolarization of several percent, and thus violate the assumption of constant depolarization ratios within the calibration region. For the example

shown here, the calibration region was chosen to be between 4.0 km (273 K) and 6.5 km (256 K), as indicated by the vertical lines in Figure 8. The mean values of the measured ratios within the calibration region are plotted for each angle in Figure 9.

7.2. DERIVING THE CALIBRATION CONSTANTS

Solutions for the calibration constants and the mean depolarization ratio were derived from these measurements using the same nonlinear least squares code that is used in the simulation software described in section 5.1. Results are presented in Table 2. The "Average of the solutions" column gives the means and standard deviations computed for all parameters when solving the calibration equation for each of the 167 sets of range-resolved measured ratios located between 4.0-km to 6.5-km. The "Solution of the averages" column gives the results obtained when the calibration equation is applied to the mean measured ratios; that is, a single application of the calibration equation for which the input data has been averaged in both time and space (i.e., as shown in Figure 9). The uncertainties reported in this second column are estimated using the technique recommended by Cox et al. (2004), as described in Section 5. The parenthetical numbers provided for the gain ratio and offset angle give the uncertainties estimated by equations (15) and (16).

7.3. DEVELOPING AN INITIAL APPROXIMATION

Numerical solutions for nonlinear least squares problems require an initial guess for each of the parameters to be derived. We have therefore developed a set of quick and easily implemented procedures that provide an excellent first approximation, $\{G_0, \delta_0, \theta_0\}$, to the desired solution vector. As illustrated in Figure 9, the relationship between the mean measured ratios and the

calibration angles can be approximated quite well using a second order polynomial. Therefore, given a quadratic approximation of measured ratios as a function of calibration angle, $m(\varphi) = C_0 + C_1 \varphi + C_2 \varphi^2$, an excellent first estimate of the offset angle is obtained by computing the negative of the minimum value of $\tilde{m}(\varphi)$ with respect to φ; i.e., $\theta_0 = {C_1}/{2C_2}$. (Note that the sign of the minimum value of the $\tilde{m}(\varphi)$ parabola will be opposite that of the offset angle.) Having computed θ_0, a gain ratio estimate, G_0, can then be generated by assuming an initial value of the depolarization ratio, δ_0, that is consistent with either prior measurements or an a priori estimate of δ_{target} (i.e., as in section 3). No great accuracy is required when estimating δ_0, as the convergence properties of the depolarization equation are quite good. We compute G_0 by solving equation (10) for gain ratio, setting $\theta = \theta_0$, $\delta = \delta_0$, then averaging over the N calibration angles; that is

$$G_0 = \frac{1}{N} \sum_{j=1}^{N} \langle m_j \rangle \cdot \left(\frac{1 + \delta_0 \cdot \tan^2\left(2\left(\theta_0 + \varphi_j\right)\right)}{\delta_0 + \tan^2\left(2\left(\theta_0 + \varphi_j\right)\right)} \right). \tag{20}$$

Here $\langle m_j \rangle$ is the mean measured ratio derived from the j^{th} calibration angle, φ_j.

7.4. SELECTION OF CALIBRATION ANGLES

Unlike G and θ, the depolarization ratio within the calibration region, δ_{target}, is not an instrument-specific constant, nor does its value or accuracy have any effect on subsequent retrievals of geophysical information. It does, however, have great intrinsic interest. Furthermore, an examination of the Monte Carlo results for δ_{target} provides useful insight into the sensitivity of the

calibration procedure to the magnitudes of the specific calibration angles chosen. In Figure 10(a) we present a contour plot showing the errors in δ_{target} as a function of SNR and N_φ, for the set of calibration angles shown in Table 1. While the depolarization ratio error decreases with increasing SNR, in a manner similar to the gain ratio and offset angle cases, the behavior with respect to an increase in N_φ is different. As evidenced by the sharp dip in the contours in Figure 10(a), relative errors in δ_{target} are clearly minimized when using only four calibration angles. Subsequent testing reveals that this behavior is a function of the particular combination of calibration angles used. The angles used for the four-angle test were ±20° and ±4°; i.e., the maximum and minimum magnitudes, placed symmetrically about zero. However, as shown in Figure 10(b), changing Table 1 and repeating the test yields very different results for errors in δ_{target}. In this trial, the calibration angles used for the three-angle test were -20°, 8°, and 16°, and the angles for the four-angle test were -20°, -12°, 12° and 16°. Errors in the retrieved depolarization ratios now fall sharply for the six-angle test, and thereafter remain relatively constant. Interestingly, the six-angle test is now the first that contains both ±20° and ±4°. Errors for G and θ in this revised test are essentially identical to those shown in Figure 3. We conclude therefore that errors in δ_{target} are sensitive to the exact combination of angles used, and that obtaining the optimum depolarization ratio results depends more on the distance spanned between the smallest and largest calibration angles (i.e., span = $\max\left(\left|\varphi_j\right|\right) - \min\left(\left|\varphi_j\right|\right)$) than on the number of angles used. This is in contrast to the behavior exhibited by the G and θ errors, for which angular span (e.g., the 4-angle case in Figure 3) was less important than total number of angles.

Additional investigations into the influence of angular span support the conclusion above, and provide addition insight into the accuracy of the gain ratio retrieval. To determine the optimum span we assumed a symmetric placement of the calibration angles, similar in all cases to the selection shown in Table 1. We then performed a series of Monte Carlo simulations for maximum magnitudes of ±9º, ±12º, ±15º, ±18º, and ±20º. A representative set of results for the four-angle case is shown in Figure 11. The RMS offset angle error is seen to remain relatively constant at ~0.3º irrespective of the angular span. As expected, the RMS depolarization ratio errors show a downward trend with increasing maximum magnitude. A linear fit to the data shown generates a slope of approximately -0.01% per degree, meaning that at an SNR of 50 we can expect to reduce the (absolute) RMS depolarization ratio error by 0.1% when using an angular span of ±20º versus a span of ±9º. Gain ratio RMS errors are also seen to decrease monotonically, by a factor of ~2, over the same 9º to 20º range.

8. SUMMARY AND CONCLUSIONS

In this work we have described a technique for obtaining the coefficients required to derive fully calibrated volume depolarization ratios from measurements made by polarization-sensitive backscatter lidars. The lidar hardware modifications necessary for implementing the calibration procedure have also been presented. While quantifying any misalignment between the polarization planes of the transmitter and receiver, this method simultaneously retrieves an accurate estimate of the system gain ratio. In contrast to previously published calibration strategies, no a priori knowledge of the molecular depolarization in the calibration region is required. Quite to the contrary, one major advantage of this new technique is that an estimate of

δ_{target} is returned as an integral part of the solution of the calibration equations. As a consequence, gain ratio calibration errors due to imprecise knowledge of the filter line width and/or other optical characteristics of the system are largely eliminated, as are errors due to aerosol contamination of assumed-to-be-clear calibration regions. Errors in subsequently derived depolarization ratios are shown to be minimized when the system offset angle is zero. The sensitivity and stability of the calibration technique has been investigated using a number of numerical simulations. High SNR measurements taken for a large number of calibration angles (e.g., $N_\varphi \geq 8$) are shown to produce the most accurate calibration coefficients. Errors in the retrieval of gain ratio and of δ_{target} are minimized when the angular distance spanned by the calibration angles is maximized. A discussion of practical considerations has been included to assist field practitioners in the efficacious implementation of the method.

ACKNOWLEDGEMENTS

The authors owe a huge debt of gratitude to Bill Fuller; without his superb design skills and logistical wizardry, the development and deployment of our polarization-sensitive lidars might never have happened. Special thanks also go to Bill Rouse for his patience and extraordinary persuasiveness with various optical apparatus.

REFERENCES

Anita, H. M., 2002: *Numerical Methods for Scientists and Engineers*. Birkhäuser Verlag, 842 pp.

Behrendt A., and T. Nakamura, 2002: Calculation of the calibration constant of polarization lidar and its dependency on atmospheric temperature. *Opt. Express*, **10**, 805-817.

Bevington, P. R. and D. K. Robinson, 1992: *Data Reduction and Error Analysis for the Physical Sciences*, McGraw-Hill, 328 pp.

Beyerle, G., M. R. Gross, D. A. Haner, N. T. Kjome, I. S. McDermid, T. J. McGee, J. M. Rosen, H.-J. Schäfer, and O. Schrems, 2001: A Lidar and Backscatter Sonde Measurement Campaign at Table Mountain during February–March 1997: Observations of Cirrus Clouds. *J. Atmos. Sci.*, **58**, 1275-1287.

Biele, J., G. Beyerle, and G. Baumgarten, 2000: Polarization lidar: Corrections of instrumental effects. *Opt. Express*, **7**, 427-435.

Bohren, C. F. and D. R. Huffman, 1983: *Absorption and Scattering of Light by Small Particles*. John Wiley & Sons, Inc., 530 pp.

Cairo, F., G. Di Donfrancesco, A. Adriani, L. Pulvirenti, and F. Fierli, 1999: Comparison of various linear depolarization parameters measured by lidar. *Appl. Opt.*, **38**, 4425-4432.

Cox, M. G., A. B. Forbes, and P. M. Harris, 2002: *Modelling and Approximation: for analysis of discrete experimental data*, in Software Support for Metrology Best Practice Guide No. 4,

National Physical Laboratory (NPL), UK, January 2002; ISSN 1471-4124; available at http://www.npl.co.uk/npl/publications/

DeCoursey, R. J., M. T. Osborn, D. M. Winker, and D. C. Woods, 1996: Recent modifications, enhancements, and measurements with an airborne lidar system. *Proc. SPIE*, **2748**, pp. 178-188.

Dennis, J. E. and R. B. Schnabel, 1996: *Numerical methods for unconstrained optimization and non-linear equations*. Society for Industrial and Applied Mathematics (SIAM), 378 pp.

Eloranta E. W. and P. Piironen, 1994: Depolarization measurements with the high spectral resolution lidar. *Abstracts of Papers, 17th International Laser Radar Conference*, Sendai, Japan, 127-128.

Frieden, B. R., 2001: *Probability, Statistical Optics, and Data Testing, 3rd Edition*, Springer-Verlag, 493 pp.

Gobbi, G. P., F. Barnaba, R. Giorgi, and A. Santacasa, 2000: Altitude-resolved properties of a Saharan dust event over the Mediterranean. *Atmos. Environ.*, **34**, 5119-5127.

Hecht, E., 2002: *Optics*, Addison-Wesley, 698 pp.

Hu, Y., D. Winker, P. Yang, B. Baum, L. Poole, and L. Vann, 2001: Identification of cloud phase from PICASSO-CENA lidar depolarization: a multiple scattering sensitivity study. *J. Quant. Spectrosc. Ra.*, **70**, 569-579.

Hull, John, technical representative, CVI Laser, LLC: private communication to JMA, 13 July 2005

McGill, M. J., D. L. Hlavka, W. D. Hart, J. D. Spinhirne, V. S. Scott, and B. Schmid, 2002: The Cloud Physics Lidar: Instrument description and initial measurement results. *Appl. Opt.*, **41**, 3725-3734.

Measures, R. M., 1984: *Laser Remote Sensing: Fundamentals and Applications*, John Wiley and Sons, Inc., 510 pp.

Murayama, T., N. Sugimoto, I. Uno, K. Kinoshita, K. Aoki, N. Hagiwara, Z. Liu, I. Matsui, T. Sakai, T. Shibata, K. Arao, B. Sohn, J. Won, S. Yoon, T. Li, J. Zhou, H. Hu, M. Abo, K. Iokibe, R. Koga, and Y. Iwasaka, 2001: Ground-based network observation of Asian dust events of April 1998 in east Asia. *J. Geophys. Res.*, **106**, 18345-18359.

Newman, P. A. and nineteen coauthors, 2002: An overview of the SOLVE/THESEO 2000 campaign. *J. Geophys. Res.*, **107**, doi:10.1029/ 2001JD001303.

Noel, V., H. Chepfer, G. Ledanois, A. Delaval, and P. H. Flamant, 2002: Classification of particle effective shape ratios in cirrus clouds based on the lidar depolarization ratio. *Appl. Opt.*, **21**, 4245-4257.

Omar, A. H., D. M. Winker, J-G. Won, M. A. Vaughan, C. A. Hostetler, and J. A. Reagan, 2003: Selection Algorithm for the CALIPSO Lidar Aerosol Extinction-to-Backscatter Ratio. *IEEE Geoscience and Remote Sensing Symposium (IGARSS) Proceedings*, **3**, 1526-1530.

Platt, C. M. R., 1977: Lidar Observation of a Mixed-Phase Altostratus Cloud. *J. Appl. Meteorol.*, **16**, 339-345.

Poole, L. R., G. S. Kent, M. P. McCormick, and W. H. Hunt, 1990: Dual-polarization airborne lidar observations of polar stratospheric cloud evolution. *Geophys. Res. Lett.*, **17**, 389-392.

Press, W. H., S. A. Teukolsky, W. T. Vetterling, and B. P. Flannery, 1992: *Numerical Recipes in C, 2nd Edition*, Cambridge University Press, 993 pp.

Sassen, K., 1991: The Polarization Lidar Technique for Cloud Research: A Review and Current Assessment. *Bull. Am. Meteorol. Soc.*, **72**, 1848-1866.

Sassen, K., 2000: Lidar Backscatter Depolarization Technique. *Light Scattering by Nonspherical Particles*, M. I. Mishchenko, J. W. Hovenier, and L. D. Travis, Eds., Academic Press, 393-416.

Sassen, K., and S. Benson, 2001: A Midlatitude Cirrus Cloud Climatology from the Facility for Atmospheric Remote Sensing. Part II: Microphysical Properties Derived from Lidar Depolarization. *J. Atmos. Sci.*, **58**, 2103-2112.

Sauvage, L., H. Chepfer, V. Trouillet, P. H. Flamant, G. Brogniez, J. Pelon, and F. Albers, 1999: Remote Sensing of Cirrus Radiative Parameters during EUCREX'94. Case Study of 17 April 1994. Part I: Observations. *Mon. Wea. Rev.*, **127**, 486-503.

Schotland, R. M., K. Sassen, and R. Stone, 1971: Observations by Lidar of Linear Depolarization Ratios for Hydrometers. *J. Appl. Meteorol.*, **10**, 1011-1017.

She, C-Y, 2001: Spectral structure of laser light scattering revisited: bandwidths of nonresonant scattering lidars. *Appl. Opt.*, **40**, 4875-4884.

Spinhirne, J. D., M. Z. Hansen, and L. O. Caudill, 1982: Cloud top remote sensing by airborne lidar. *Appl. Opt.*, **21**, 1564-1571.

Starr, D. O'C., T. P. Ackerman, S. A. Ackerman, W. Cotton, S. K. Cox, A. J. Heymsfield, D. S. McDougal, K. Sassen, A. Slingo, W. L. Smith, G. L. Stephens, C. H. Whitlock, B. A. Wielicki, and D. P. Wylie, 1990: *FIRE Phase II: Cirrus Implementation Plan*, available at http://asd-www.larc.nasa.gov/fire/FIRE_II/Cirrus_Imp_Plan_1990.html

Toon, O. B., A. Tabazadeh, E. V. Browell, and J. Jordan, 2000: Analysis of lidar observations of Arctic polar stratospheric clouds during January 1989. *J. Geophys. Res.*, **105**, 20589-20615.

Winker D. M. and M. T. Osborn, 1992: Preliminary analysis of observations of the Pinatubo volcanic plume with a polarization-sensitive lidar. *Geophys. Res. Lett.*, **19**, 171-174.

Winker D. M. and M. A. Vaughan, 1994: Vertical distribution of clouds over Hampton, Virginia observed by lidar under the ECLIPS and FIRE ETO programs, *Atmos. Res.*, **34**, 117-133.

Winker, D. M., J. Pelon, and M. P. McCormick, 2003: The CALIPSO mission: Spaceborne lidar for observation of aerosols and clouds", *Proc. SPIE*, **4893**, 1-11.

FIGURE CAPTIONS

Figure 1: Schematic diagram of a dual polarization backscatter lidar (components not drawn to scale). The design shown here is for the LaRC 8" Cloud Lidar, originally built in 1987, and used continuously through 1994 for cirrus cloud measurements as part of the FIRE program. Additional detail can be found in Winker and Vaughan (1994) and in Decoursey et al. (1996)

Figure 2: Aligned and misaligned receiver geometries; the left-hand panel shows a perfectly aligned configuration; the center panel shows the position of the laser polarization vector for transmitter-receiver misalignment angle of θ in a receiver with no half-wave plate; the right-hand panel shows the position of the laser polarization vector for the misalignment angle in a receiver having a half-wave plate with its principal axis co-aligned with the parallel axis of the PBS. Note that if the half-wave plate axis were rotated counter-clockwise by an angle of $\theta/2$, the laser polarization vector would be in alignment with the parallel axis of the PBS.

Figure 3: Gain ratio (left) and offset angle (right, in degrees) RMS errors as functions of signal-to-noise ratio and the number of calibration angles used derived assuming error-free calibration angles. The SNR axis is plotted on a log scale, while the N_φ axis uses a linear scale. Errors retrieved from the simulation were computed using equation (11), and are shown using solid lines. The dashed lines represent error estimates computed using equations (12) (gain ratio) and (13) (offset angle).

Figure 4: Gain ratio (left) and offset angle (right, in degrees) RMS errors as functions of signal-to-noise ratio and the number of calibration angles used derived for calibration angles having an uncertainty of 38.3 μrad. The SNR axis is plotted on a log scale, while the N_φ axis uses a linear scale. Errors retrieved from the simulation were computed using equation (11), and are shown using solid lines. The dashed lines represent error estimates computed using equations (15) (gain ratio) and (16) (offset angle).

Figure 5: Four-angle simulation results; G=2.5, δ=1.44%; θ=0.2º

Figure 6: Relative error in depolarization ratio as a function of uncertainties in offset angle and gain ratio for θ = 0.1° (left), θ = 1.0° (center), and θ = 2.5° (right). For all plots, the measured ratio SNR was maintained at a fixed value of 50.

Figure 7: (a) Gain ratios determined by the normalization technique (see section 3) for a nominal gain ratio of 1.00 and a range of offset angles spanning ±2° for both narrow band (Cabannes scattering only) and broad band (Rayleigh scattering) filters; (b) relative error in the depolarization ratios retrieved using equation (4) for a system with a broad band filter and an offset angle of 1°; the dashed line indicates errors incurred when the correct gain ratio (G = 1) is used; the solid line indicates errors incurred when the gain ratio that would be derived via the normalization technique (G = 1.085) is used.

Figure 8: Measured ratios acquired by the LaRC 8" Cloud Lidar on 12 November 1991. The lowest values for the measured ratios are acquired at the smallest calibration angles. Data acquired for negative calibration angles is plotted using dashed lines; data acquired using positive calibration angles is plotted with solid lines.

Figure 9: Mean value of the measured ratios, $\langle m_j \rangle$, at each calibration angle, φ_j, computed over the calibration region indicated in Figure 8 (4.0-km to 6.5km). Error bars in this figure represent ±3 standard deviations about the mean. The dotted line represents the quadratic approximation used to generate an initial guess for the offset angle. The minimum of this quadratic provides the initial guess for offset angle required by the nonlinear least squares algorithm. The solid curve is computed using equation (9) and the retrieved calibration coefficients specified in Table 2.

Figure 10: (a) Depolarization ratio RMS errors (i.e., as in equation (11)) as functions of SNR and N_φ for the calibration angles given in Table 1; (b) as in (a), but using calibration angles of -20°, 8°, and 16° for the three-angle test, and -20°, -12°, 12° and 16° for the four-angle test.

Figure 11: RMS errors for gain ratio, depolarization ratio, and offset angle as functions of increasing angular span. All calibrations were conducted using 4 calibration angles and a uniform backscatter SNR of 50.

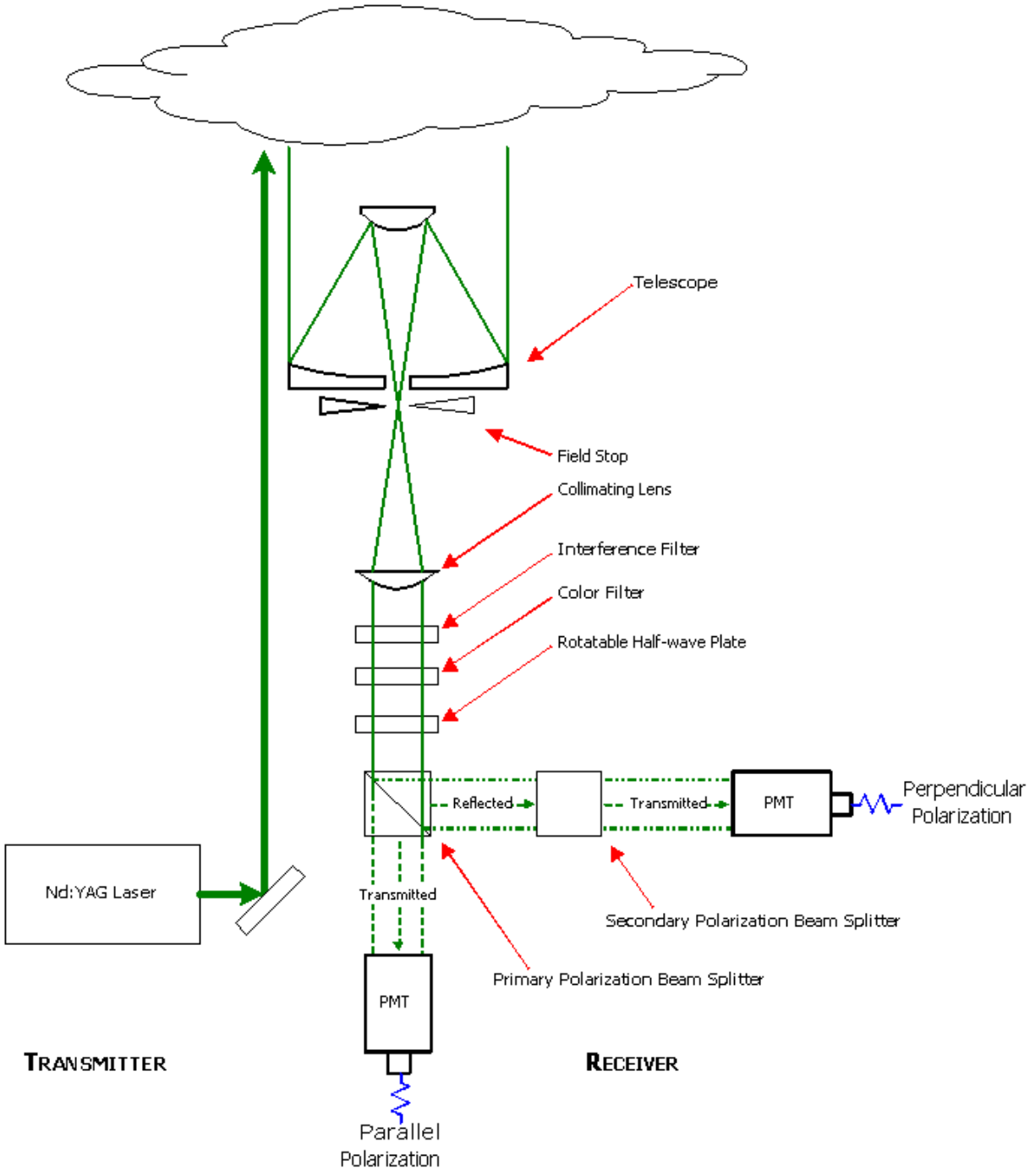
Telescope
Field Stop
Collimating Lens
Interference Filter
Color Filter
Rotatable Half-wave Plate
Reflected
Transmitted
PMT
Perpendicular Polarization
Nd:YAG Laser
Transmitted
Secondary Polarization Beam Splitter
Primary Polarization Beam Splitter
PMT
TRANSMITTER
RECEIVER
Parallel Polarization

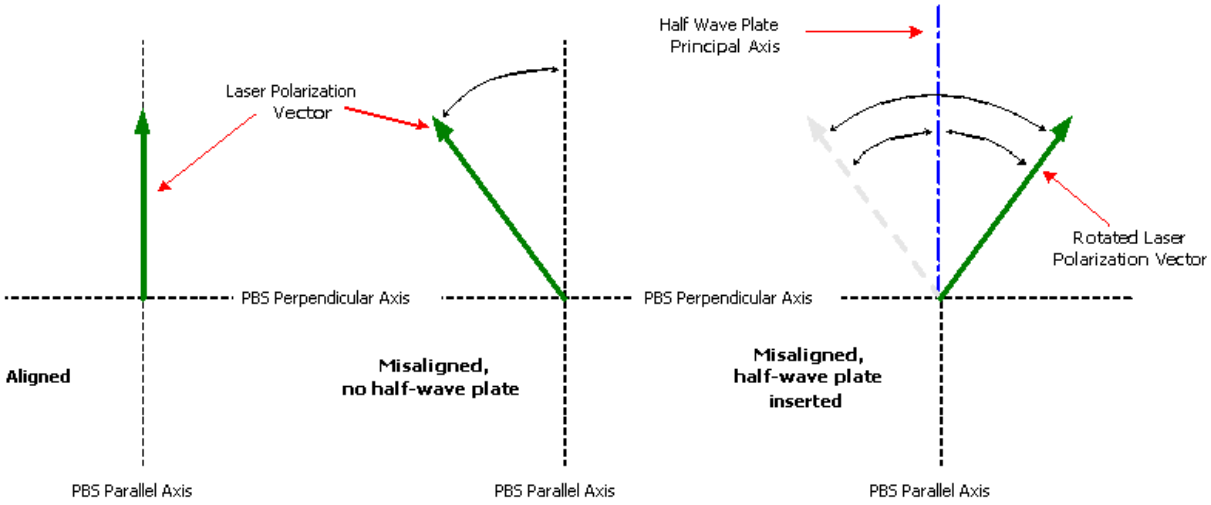
Laser Polarization
Vector
PBS Perpendicular Axis
Aligned
PBS Parallel Axis
Misaligned,
no half-wave plate
PBS Parallel Axis
Half Wave Plate
Principal Axis
PBS Perpendicular Axis
Misaligned,
half-wave plate
inserted
Rotated Laser
Polarization Vector
PBS Parallel Axis

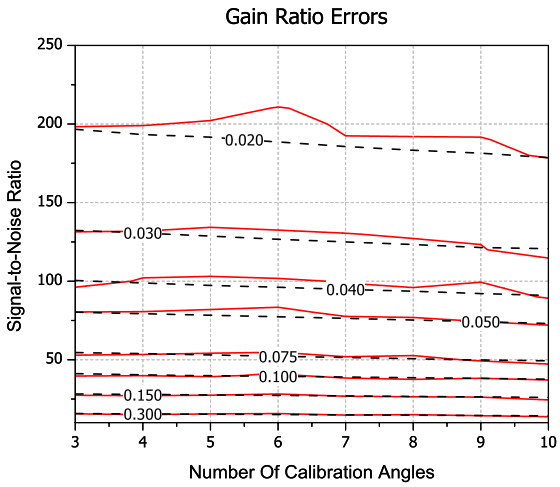
Gain Ratio Errors
Signal-to-Noise Ratio
Number Of Calibration Angles
250
200
150
100
50
3
4
5
6
7
8
9
10
0.020
0.030
0.040
0.050
0.075
0.100
0.150
0.300

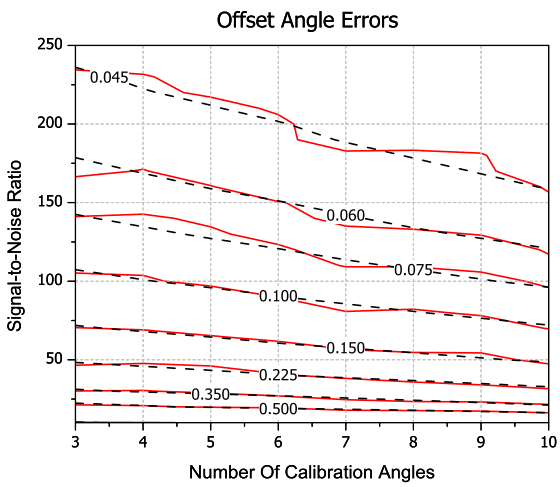
Offset Angle Errors
Signal-to-Noise Ratio
Number Of Calibration Angles
250
200
150
100
50
3
4
5
6
7
8
9
10
0.045
0.060
0.075
0.100
0.150
0.225
0.350
0.500

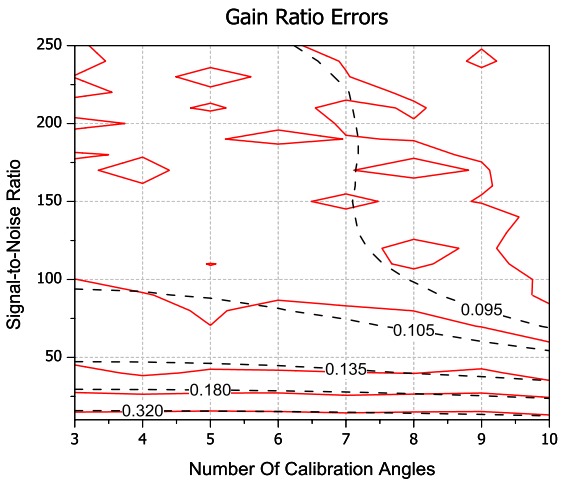
Gain Ratio Errors
Signal-to-Noise Ratio
Number Of Calibration Angles
250
200
150
100
50
3
4
5
6
7
8
9
10
0.095
0.105
0.135
0.180
0.320

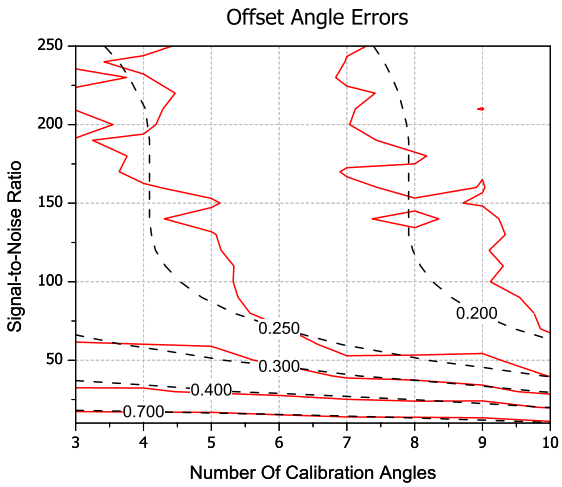
Offset Angle Errors
Signal-to-Noise Ratio
Number Of Calibration Angles
250
200
150
100
50
3
4
5
6
7
8
9
10
0.200
0.250
0.300
0.400
0.700

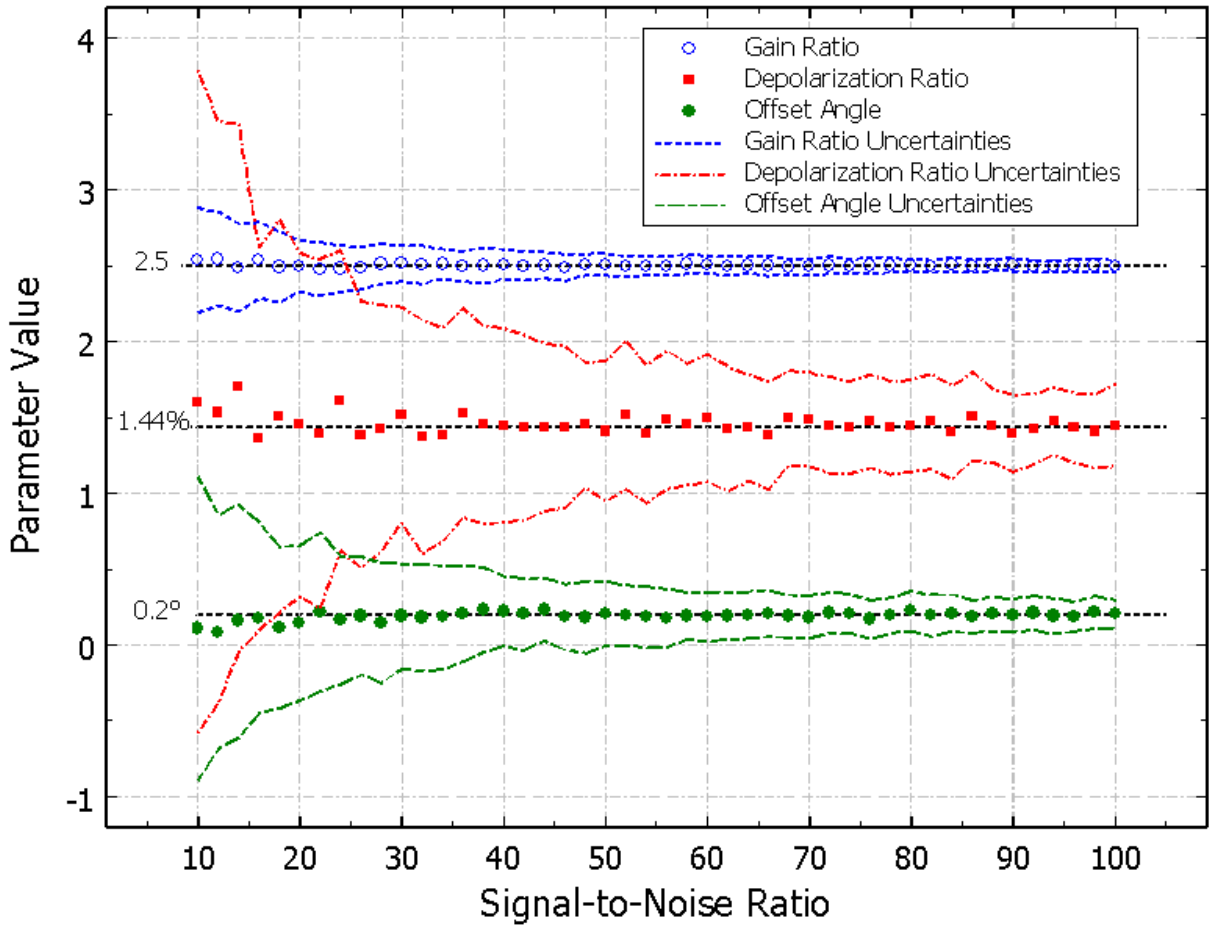
Gain Ratio
Depolarization Ratio
Offset Angle
Gain Ratio Uncertainties
Depolarization Ratio Uncertainties
Offset Angle Uncertainties
2.5
1.44%
0.2°
Parameter Value
Signal-to-Noise Ratio
4
3
2
1
0
-1
10
20
30
40
50
60
70
80
90
100

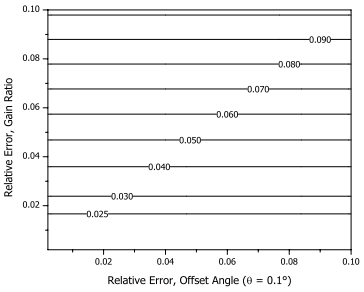
Relative Error, Gain Ratio
Relative Error, Offset Angle (θ = 0.1°)
0.090
0.080
0.070
0.060
0.050
0.040
0.030
0.025

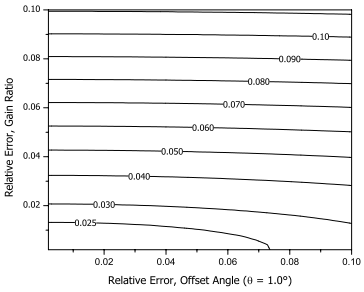
Relative Error, Gain Ratio
Relative Error, Offset Angle (θ = 1.0°)
0.10
0.090
0.080
0.070
0.060
0.050
0.040
0.030
0.025

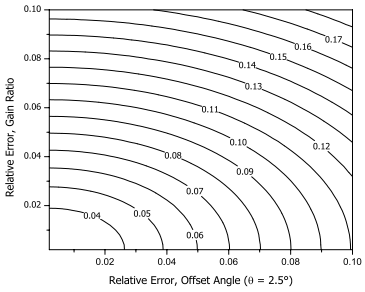
Relative Error, Gain Ratio
Relative Error, Offset Angle (θ = 2.5°)
0.17
0.16
0.15
0.14
0.13
0.11
0.10
0.12
0.08
0.09
0.07
0.04
0.05
0.06

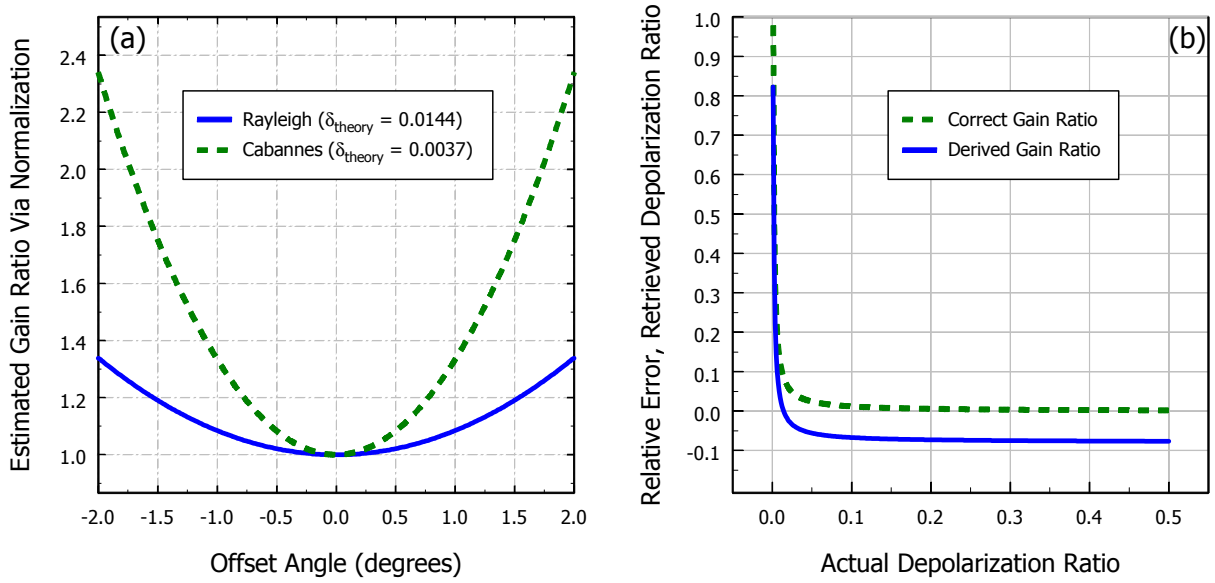
(a)
Estimated Gain Ratio Via Normalization
Offset Angle (degrees)
Rayleigh (δtheory = 0.0144)
Cabannes (δtheory = 0.0037)
2.4
2.2
2.0
1.8
1.6
1.4
1.2
1.0
-2.0
-1.5
-1.0
-0.5
0.0
0.5
1.0
1.5
2.0
(b)
Relative Error, Retrieved Depolarization Ratio
Actual Depolarization Ratio
Correct Gain Ratio
Derived Gain Ratio
1.0
0.9
0.8
0.7
0.6
0.5
0.4
0.3
0.2
0.1
0.0
-0.1
0.0
0.1
0.2
0.3
0.4
0.5

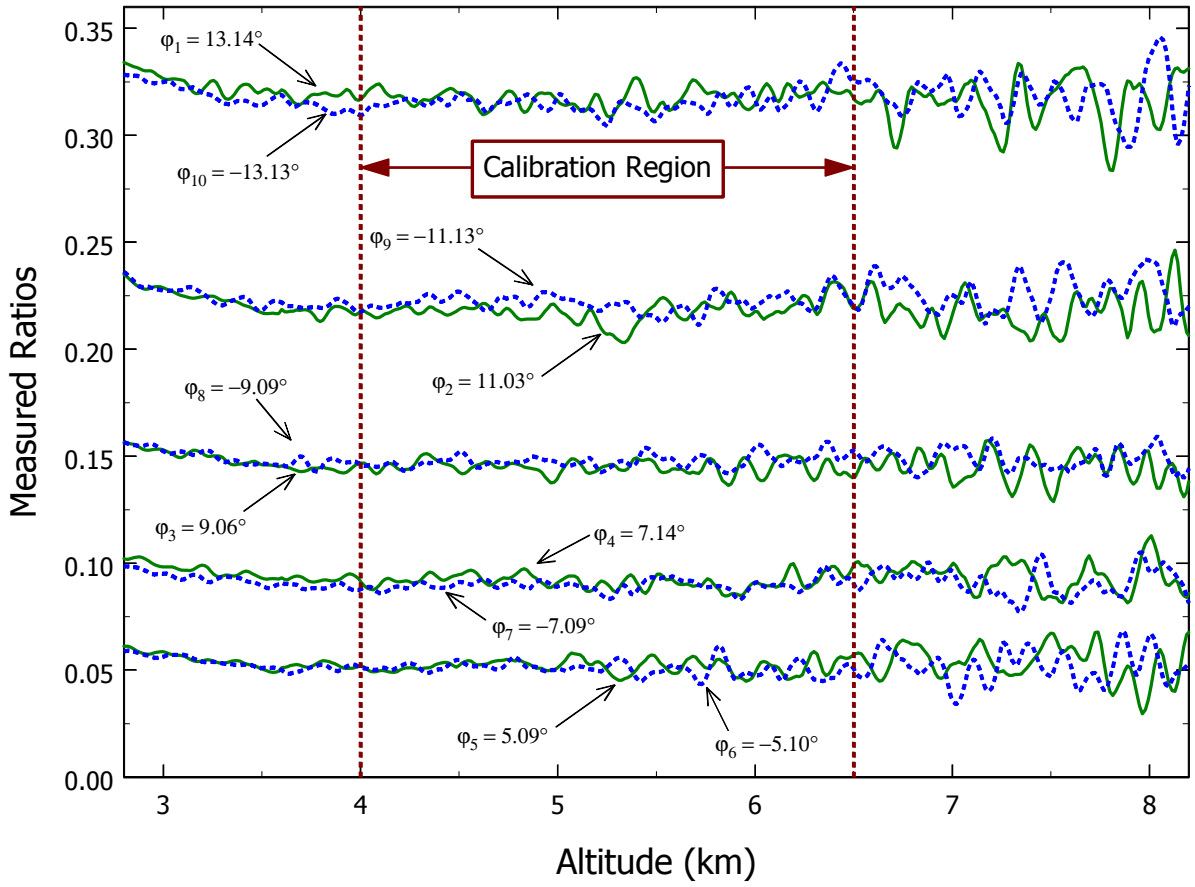
Measured Ratios
Altitude (km)
Calibration Region
φ1 = 13.14°
φ10 = −13.13°
φ9 = −11.13°
φ2 = 11.03°
φ8 = −9.09°
φ3 = 9.06°
φ4 = 7.14°
φ7 = −7.09°
φ5 = 5.09°
φ6 = −5.10°
0.00
0.05
0.10
0.15
0.20
0.25
0.30
0.35
3
4
5
6
7
8

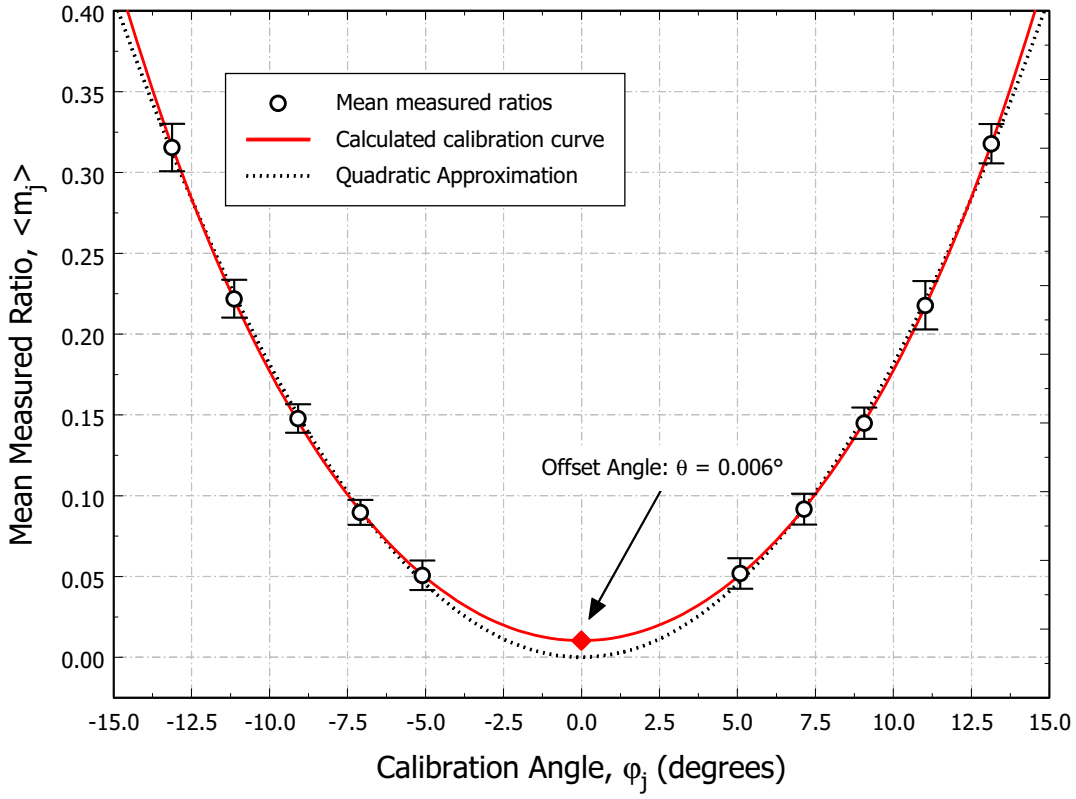
Mean measured ratios
Calculated calibration curve
Quadratic Approximation
Offset Angle: θ = 0.006°
Mean Measured Ratio, <mj>
Calibration Angle, φj (degrees)
0.40
0.35
0.30
0.25
0.20
0.15
0.10
0.05
0.00
-15.0
-12.5
-10.0
-7.5
-5.0
-2.5
0.0
2.5
5.0
7.5
10.0
12.5
15.0

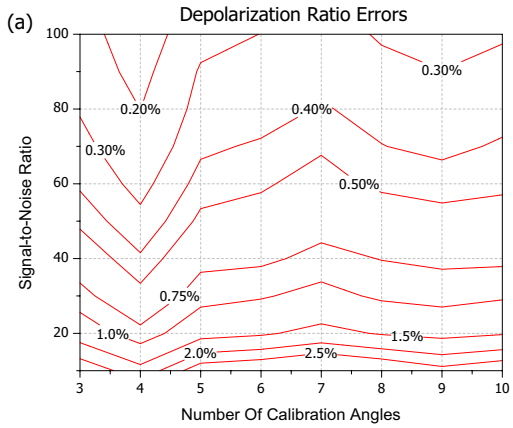
(a)
Depolarization Ratio Errors
Signal-to-Noise Ratio
Number Of Calibration Angles
0.20%
0.30%
0.40%
0.50%
0.75%
1.0%
1.5%
2.0%
2.5%
100
80
60
40
20
3
4
5
6
7
8
9
10

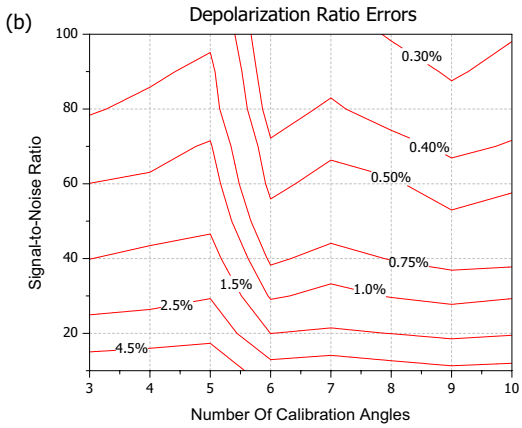
(b)
Depolarization Ratio Errors
Signal-to-Noise Ratio
Number Of Calibration Angles
0.30%
0.40%
0.50%
0.75%
1.0%
1.5%
2.5%
4.5%
100
80
60
40
20
3
4
5
6
7
8
9
10

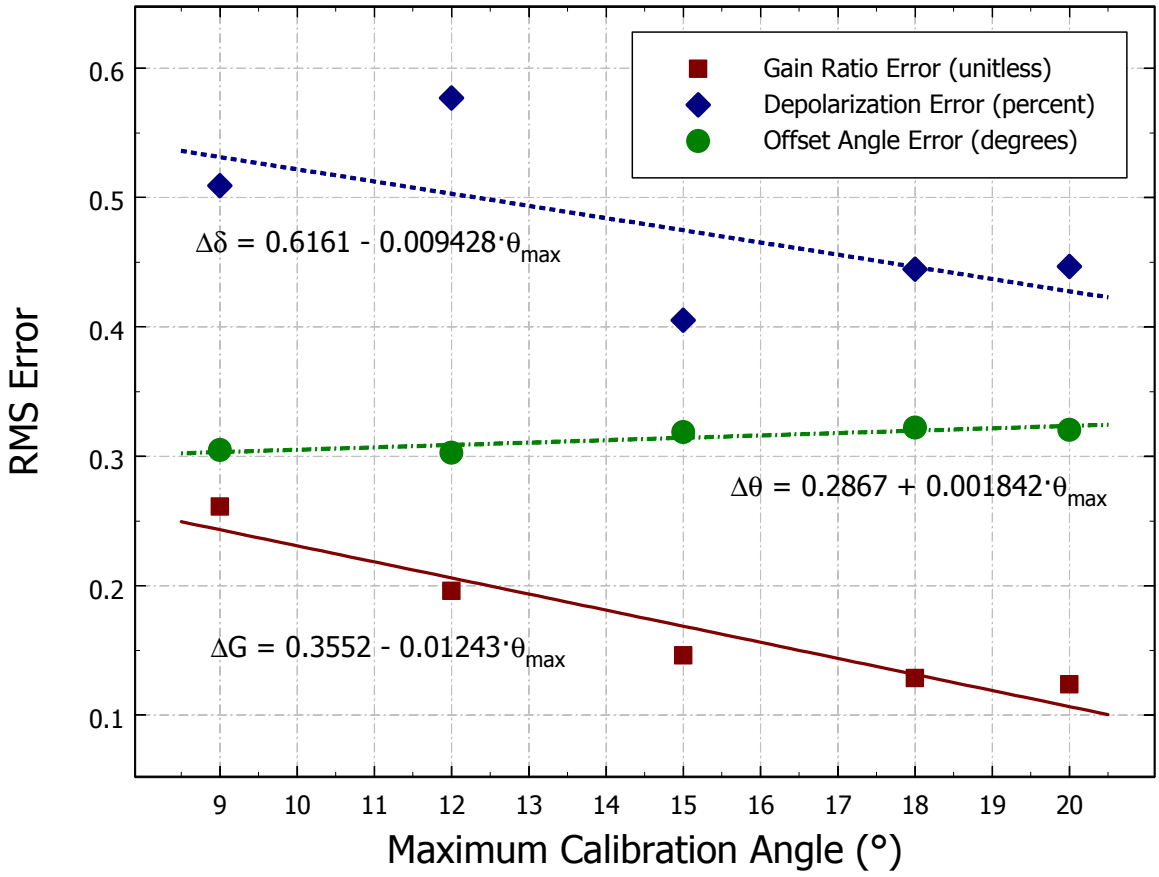
Gain Ratio Error (unitless)
Depolarization Error (percent)
Offset Angle Error (degrees)
Δδ = 0.6161 - 0.009428·θmax
Δθ = 0.2867 + 0.001842·θmax
ΔG = 0.3552 - 0.01243·θmax
RMS Error
0.6
0.5
0.4
0.3
0.2
0.1
9
10
11
12
13
14
15
16
17
18
19
20
Maximum Calibration Angle (°)

Table 1: Calibration angles, φ, used in the Monte-Carlo study; the actual angles used in each phase of the study is indicated with an "x" in the appropriate columns of the table

N_φ	-20º	-16º	-12º	-8º	-4º	4º	8º	12º	16º	20º
n = 3	x				x					x
n = 4	x				x	x				x
n = 5	x		x		x	x				x
n = 6	x		x		x	x		x		x
n = 7	x	x	x		x	x		x		x
n = 8	x	x	x		x	x	x	x		x
n = 9	x	x	x	x	x	x	x	x		x
n = 10	x	x	x	x	x	x	x	x	x	x

Table 2: Calibration constants derived for the LaRC 8" Cloud Lidar measurements obtained on 12 November 1991

	Average of the solutions	Solution of the averages
Gain Ratio	1.262 ± 0.019	1.262 ± 0.007 (0.084)
Offset Angle (degrees)	0.006 ± 0.031	0.006 ± 0.016 (0.171)
Depolarization Ratio (%)	0.820 ± 0.172	0.818 ± 0.089